Chapter 5

Model validation

The goal of this chapter is to validate the model developed in this work, and to demonstrate its feasibility in performing active noise control studies.

5.1 Fan noise model validation

In order to validate the two fan models derived in this work, results obtained with each model are compared to experimental data. The experimental data used as reference represent the directivity of the far field sound pressure radiating from the inlet of a Pratt and Whitney JT15D turbofan engine (Smith et al. 1997). These data (presented in Figure 5.1) were collected during an experiment in which the first order circumferential modes (1,0), (1,1) and (1,2) were excited to dominance and radiated into the far field of the inlet. The acoustic field of the JT15D engine was monitored with an array of nineteen far field microphones positioned in the horizontal plane passing through the centerline of the engine. The microphones were spaced along an arc of radius 1.6 m at 10 degree increments to obtain the acoustic directivity from -90 degrees to 90 degrees, where 0 degrees is along the inlet axis.

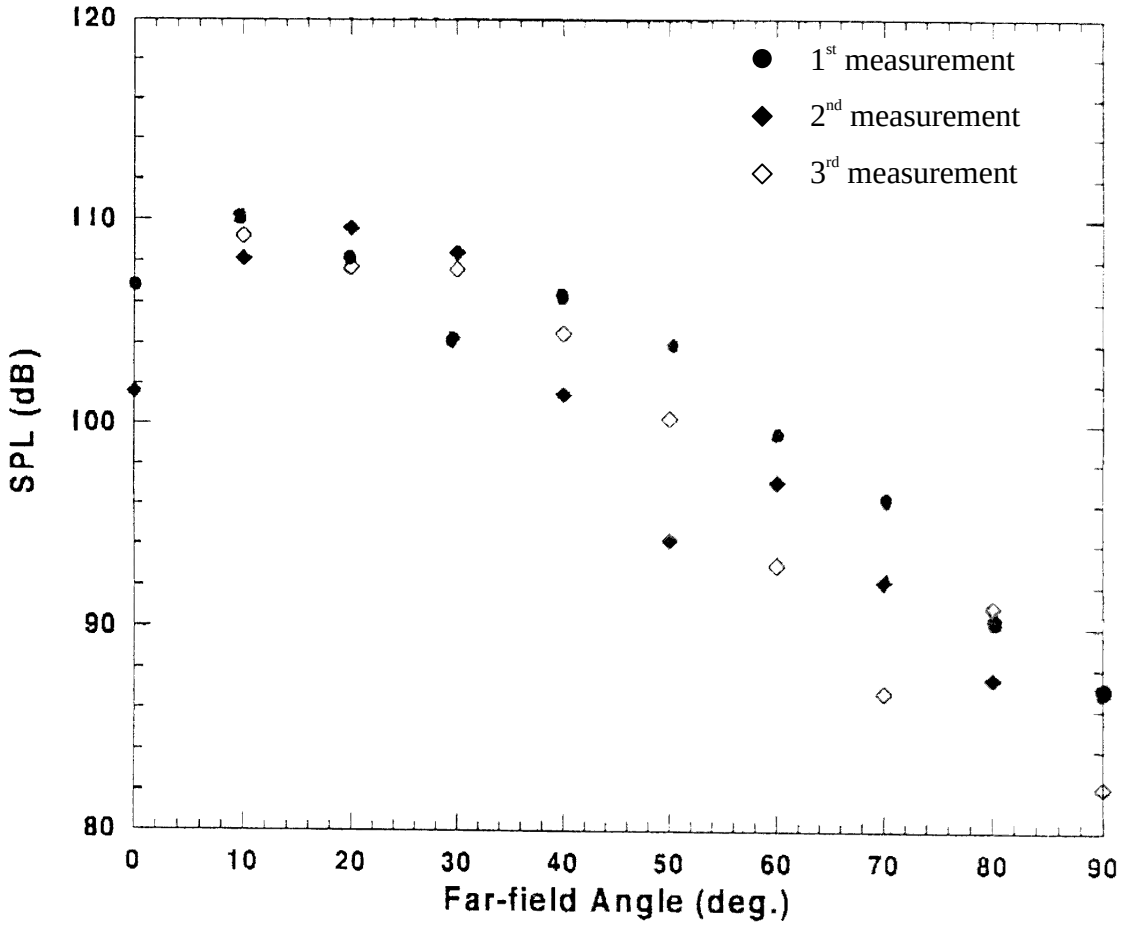

Figure 5.1: Directivity of the far field sound pressure radiating from the inlet of a JT15D turbofan engine. Experimental measurements.

The engine geometry and operating conditions used in that experiment, as well as the complex amplitudes of the propagating modes, are listed below:

Duct radius	0.26 m
Inlet length	0.6 m
Outlet length	1.2 m
Flow Mach number	0.12

Blade passage frequency	2320 Hz
Modal amplitude $A_{1,0}$	0.428E-3 – i 0.160E-2
Modal amplitude $A_{1,1}$	0.102E-2 + i 0.149E-2
Modal amplitude $A_{1,2}$	-0.166E-3 – i 0.185E-2

These parameters were used in order to simulate the operating conditions during the experiment. The resulting acoustic directivity predicted with each fan model is presented next.

5.1.1 Radial arrays of spinning point dipoles

A single radial array of point dipoles was used in order to model the generation of first order circumferential modes. The radial array was composed of fifteen point dipoles evenly distributed along the duct radius. The first point dipole was located at the radial location $r_1 = 0.06\ r_d$ (where r_d is the duct radius) while the last point dipole was located at $r_{15} = 0.94\ r_d$. In order to simulate the generation of the (1,0), (1,1) and (1,2) modes with modal amplitudes $A_{1,0}$, $A_{1,1}$ and $A_{1,2}$, the procedure described in section 3.2.2 was followed. The pressure was computed along an arc of radius 1.6 m located in front of the duct inlet as shown in Figure 5.2. The acoustic pressure generated by each point dipole of unit strength was first computed, thus obtaining the matrix $[P^0]$. The acoustic pressure resulting from the radiation of the (1,0), (1,1) and (1,2) modes of modal amplitudes $A_{1,0}$, $A_{1,1}$ and $A_{1,2}$ was then obtained by multiplying the matrix $[P^0]$ by the vector of dipole strengths defined by

$$q(j) = A_{1,0}\, J_1\left(k_r^{1,0}\ r_j\right) + A_{1,1}\, J_1\left(k_r^{1,1}\ r_j\right) + A_{1,2}\, J_1\left(k_r^{1,2}\ r_j\right)$$

$$= A_{1,0}\, J_1\left(\frac{1.84}{r_d} r_j\right) + A_{1,1}\, J_1\left(\frac{5.33}{r_d} r_j\right) + A_{1,2}\, J_1\left(\frac{8.54}{r_d} r_j\right) \qquad (5.1)$$

where j=1,…,15. Referring to section 3.1, 1.84, 5.33 and 8.54 are the first three zeros of $\frac{d}{dr}(J_1(r))$.

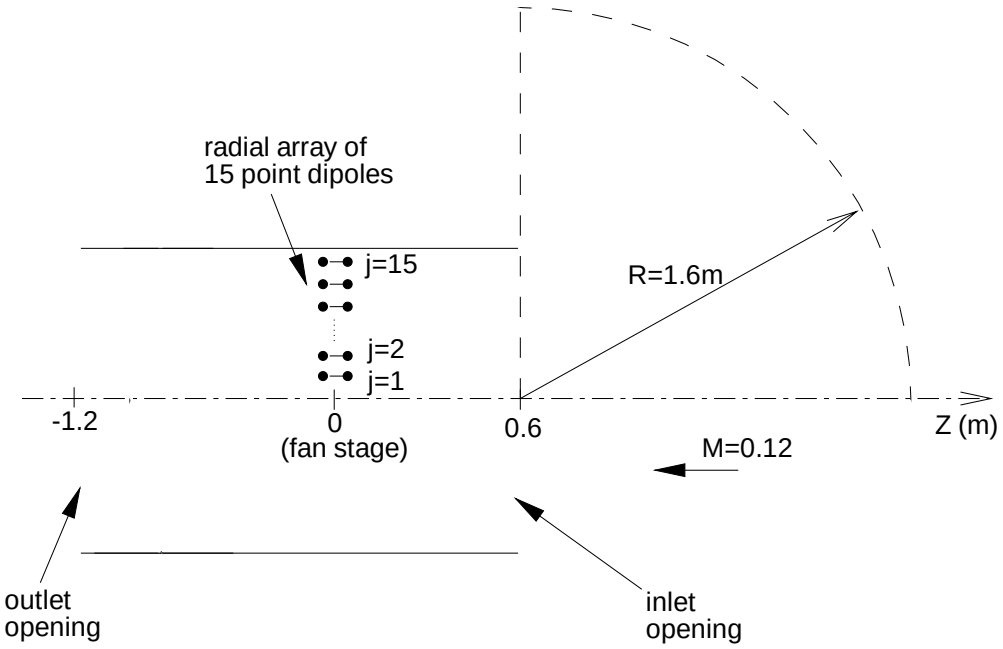

Figure 5.2: Schematic for fan model validation. Radial array of spinning point dipoles.

The directivity of the computed acoustic pressure is compared in Figure 5.3 to the experimental data. It is observed that experimental and numerical results match well at the angles of the far field where experimental data were available. Experimental and numerical results only seem to differ by a few decibels at approximately 90 degrees. This discrepancy could be caused by differences in duct inlet edge geometry between the real

engine and the model. In the case of the JT15D engine, the edge of the inlet wall is rounded and of finite thickness, while in the numerical model the edge of the duct inlet is infinitesimally thin and sharp. As a result, the complex diffraction phenomena that takes place at the edge of the duct inlet wall is different for both cases.

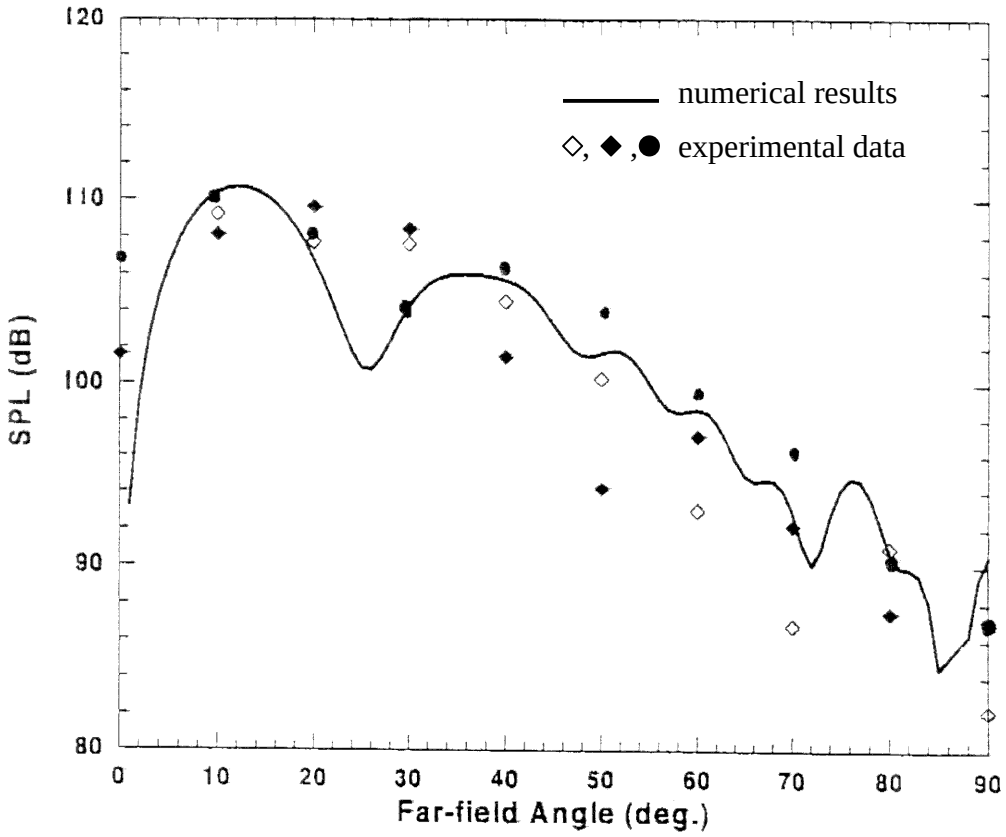

Figure 5.3: Comparison of numerical results to experimental data.
Fan model based on spinning point dipoles.

However, despite some small discrepancies at high angles of radiation, the fan model can be seen to provide a good simulation of real engine fan noise radiation.

5.1.2 Spinning line sources

With this fan model, the radial distribution of the strength of the spinning line sources generating the fan noise has to be representative of the radial distribution $\vec{F}(r)$ of the loading force along the fan blades. However, this distribution is not known for the JT15D experiment. Figure 5.4, taken from Dring et al. (1982), depicts a typical radial distribution of the force exerted by the air on the blade of a fan. The data are shown in terms of the axial and tangential components of the force per unit span (F_z and F_ψ), and the total force per unit span (F), for different engine operating conditions. Based on these plots, the radial distribution of the loading force $\vec{F}(r)$ was approximated with a linear distribution of the form

$$\vec{F}(r) = F_\psi(r)\,\hat{i}_\psi + F_Z(r)\,\hat{i}_Z$$

$$= (a\,r + b)\,\hat{i}_\psi + (c\,r + d)\,\hat{i}_Z, \quad 0 \le \frac{r}{r_d} \le 0.98 \qquad (5.2)$$

The acoustic pressure directivity obtained with this fan model is compared to the one obtained previously with the fan model based on spinning point dipoles in Figure 5.5. These two directivity plots show a similar trend, i.e., they both have peaks at the same far field angles. However, these peaks have slightly different amplitudes. This was expected since the energy distribution within the radial modes depends, in a complex manner, on the radial distribution of the blade loading (Kraft and Kontos 1993). Replacing the function defined by Eq. (5.2) with

$$\vec{F}(r) = \begin{cases} (a\,r + b)\,\hat{i}_{\psi} + (c\,r + d)\,\hat{i}_{Z}, & 0 \le \dfrac{r}{r_d} \le 0.8 \\ (-a'r)\,\hat{i}_{\psi} + (-c'r)\,\hat{i}_{Z}, & 0.8 \le \dfrac{r}{r_d} \le 0.98 \end{cases} \tag{5.3}$$

which is a function that more closely represents the radial distribution of the loading force depicted in Figure (5.4), did not lead to any significant improvements.

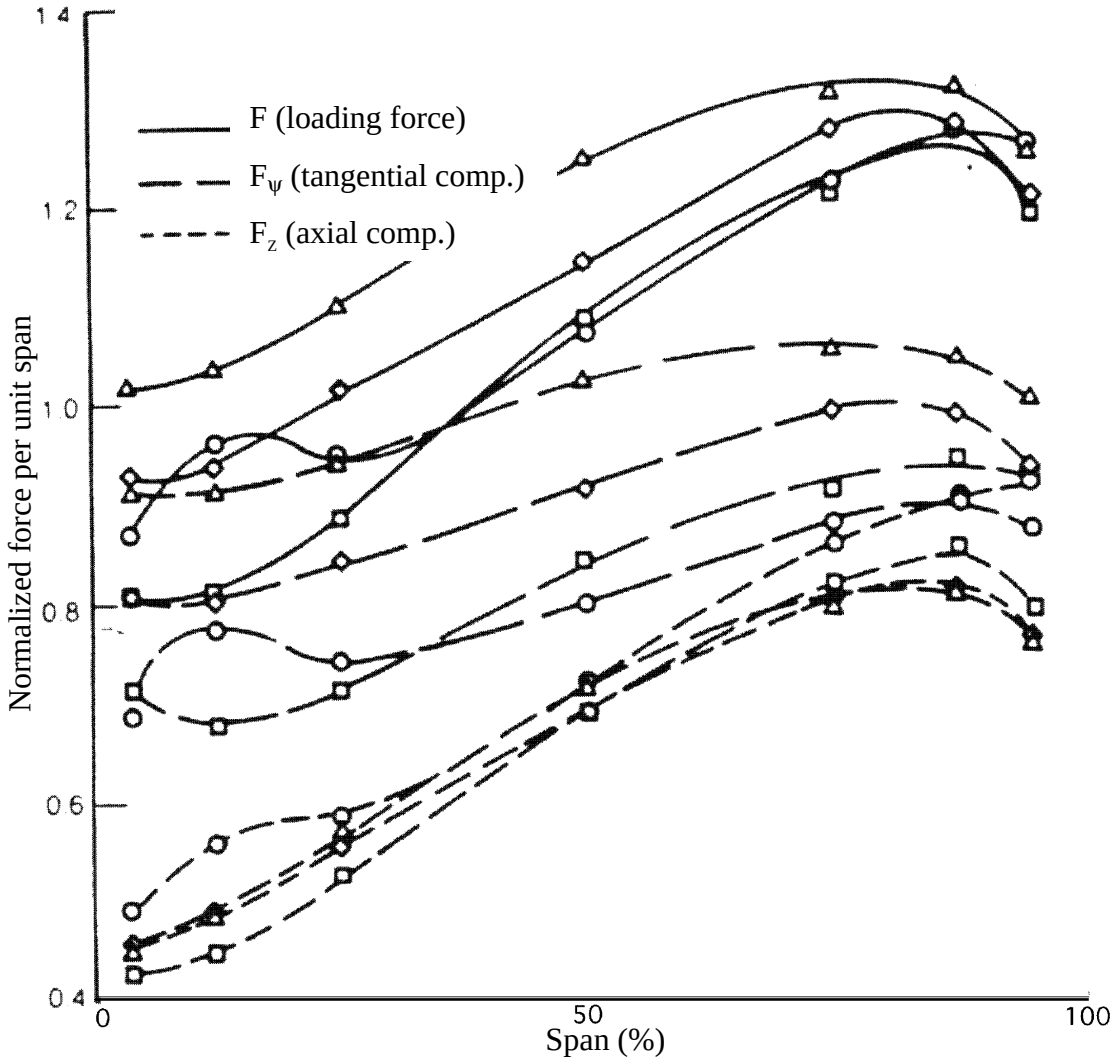

Figure 5.4: Fan loading force variations with blade span (taken from Dring 1982).

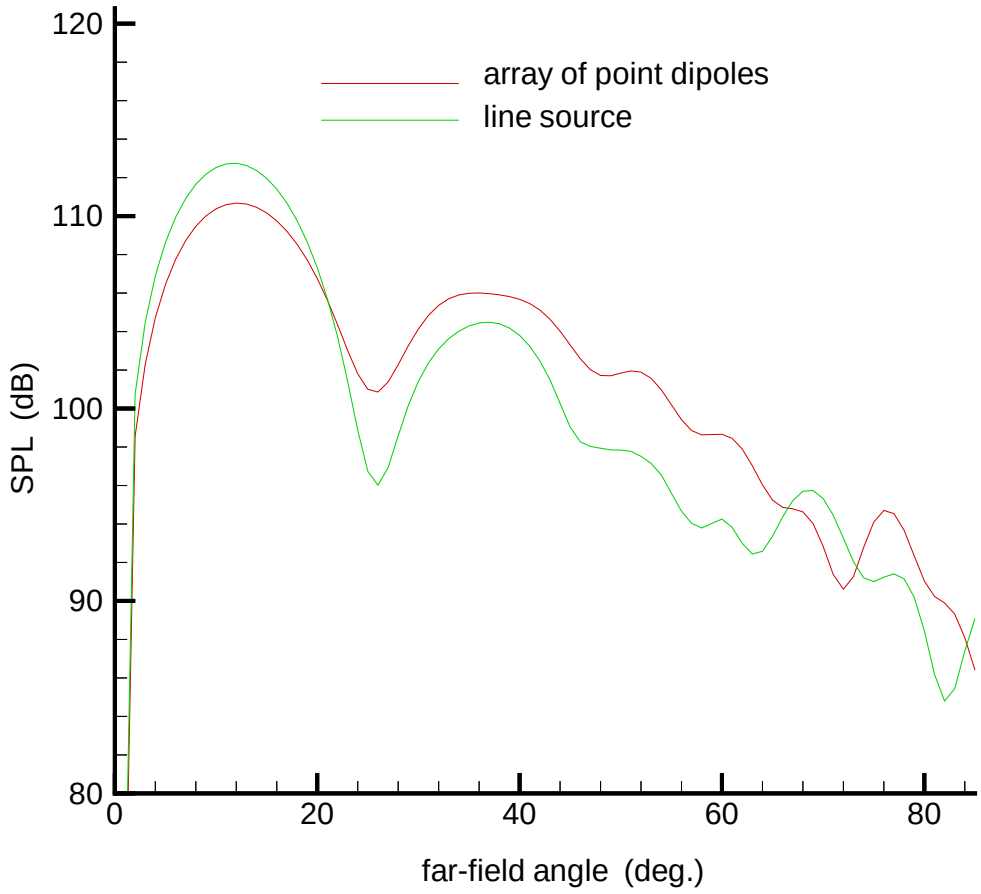

Figure 5.5: Comparison of the radiation directivity obtained with the fan model using line sources and the fan model using radial arrays of point dipoles.

The good agreement between the predicted and experimental results presented in sections 5.1.1 and 5.1.2 validate the analytical derivation and the numerical implementation of the two fan models considered in this study. It also shows that these fan models can provide a good simulation of actual engine fan noise radiation.

5.2 Control source model verification

Since suitable experimental data does not seem to be available in the open literature, verification of the analytical expression derived for the field generated by a point monopole (i.e., control source) was performed by comparing the radiation directivity of the far field sound pressure generated by two closely located point monopoles of opposite strength to the one generated by a point dipole. The pressure field generated by the reference point dipole was obtained by running the ducted fan noise prediction code TBIEM3D with its original fan model. This original fan model was chosen as a reference since it was used in several studies (Dunn et al. 1996, Dunn and Farassat 1998, Posey et al. 1998) and used the analytical expression for the pressure field generated by a single (or a collection of) point dipole(s) placed inside a duct.

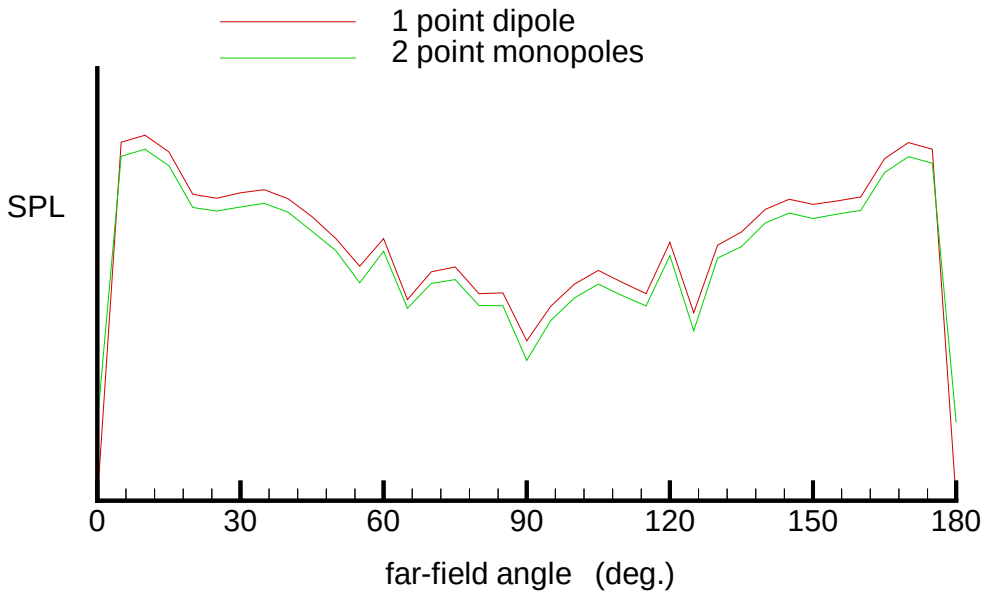

Figure 5.6: Comparison of the radiation directivity generated by a point dipole and by two point monopoles of opposite strengths placed inside the duct.

The duct geometry and flow Mach number modeled in section 5.1 were again used to perform this verification. A point monopole of strength q was placed at the axial location z = 0.5 cm, while a point monopole of strength -q was placed at z = -0.5 cm. Both point monopoles were located at a radial distance of 0.25 m from the duct axis. The resulting far field sound pressure radiating from the inlet and outlet of the duct was measured in a plan containing the duct axis, over an arc of radius 3 m, centered on the axis of the duct at z =0 m, and extending from 0 to 180 degrees as measured from the inlet axis. These results were compared to the ones obtained when the two point monopoles were replaced by a single point dipole placed at z = 0 m and 0.25 m from the axis of the duct. A comparison of the two far field sound pressure plots is presented in Figure 5.6. Note from this figure that the directivity of both fields is practically identical, thus verifying the derivations made in Chapter 4 to obtain the analytical expression of the pressure field generated by a point monopole placed inside a duct.

5.3 Demonstrative cases of Active Noise Control

Some simple cases of active noise control were performed to demonstrate the feasibility of the method used in this work. In each of the cases that are presented, a duct of cylindrical shape and finite length is considered. The duct length L is 2 m, the inlet length is 1m and the inlet diameter to length ratio is 2, which is representative of the dimensions of the inlet of a large turbofan engine. The generation and control of first order circumferential modes is modeled. A single point dipole spinning in the center of the duct is used to generate these disturbance (fan) modes. Control of inlet and/or outlet radiation was achieved using one or two arrays of control sources and error sensors placed in the far field of the duct inlet and outlet.

In each of the first three cases presented, the goal of the active control system is to minimize the sound power radiating from the *inlet* of the duct. The power level of the sound radiating from the duct inlet is computed by integrating the intensity over a hemisphere placed in front of the open section of the inlet as sketched in Figure 5.7. Also, to permit an easier identification of the factors that might influence the performance of the control system, only one or two modes, the (1,0) and (1,1) modes, will assumed to be propagating in the duct.

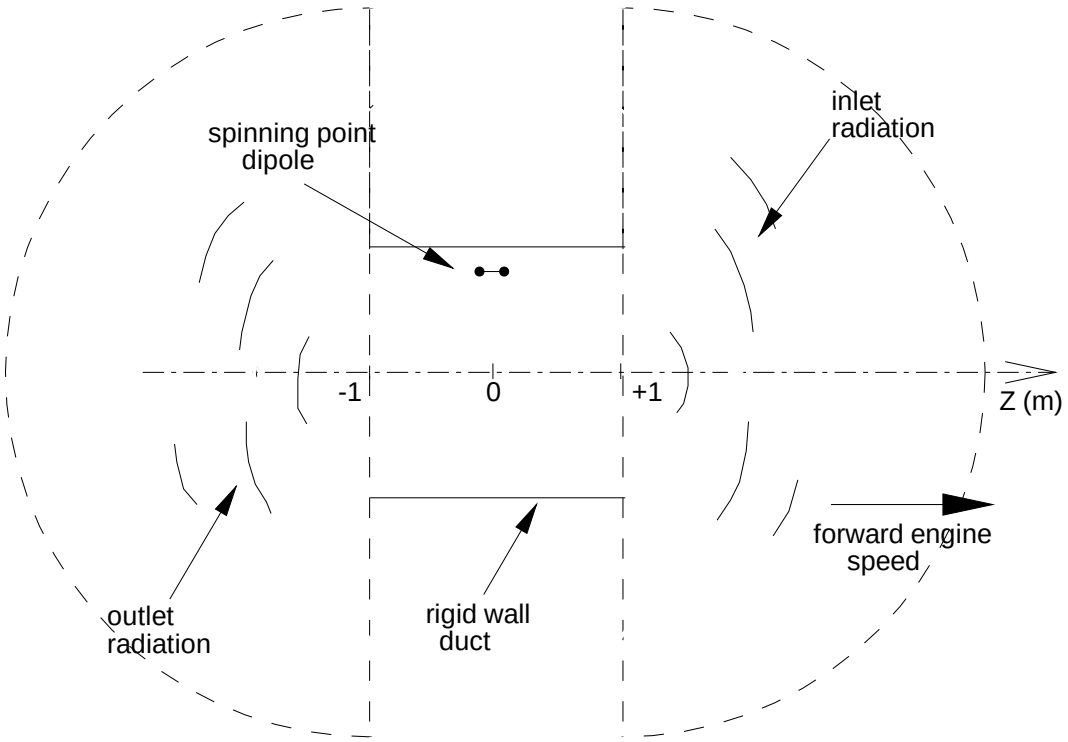

Figure 5.7: Schematic of the ducted fan considered for the demonstrative cases of active noise control.

5.3.1 Stationary duct with a single array of control sources

In this first case, the ducted fan is considered stationary and the spinning point dipole modeling the fan noise spins with a frequency (blade passage frequency) of 270 Hz, such that only the (1,0) mode is cut on.

The pressure field generated by the ducted fan in a plane containing the axis of the duct (18,856 point locations) is computed on a PC (Pentium 2, 300 Mhz processor and 32 MB of RAM) in approximately 5 minutes. The resulting in-duct and radiated fields, which are both axisymmetric, are presented in Figure 5.8(a). In this figure, the out-of-phase pressure pattern generated by the pulsating point dipole (used to model the fan noise) can clearly be seen in the center of the duct, close to the duct wall. Also, since the duct is stationary and the fan (i.e., the spinning point dipole) is located in the middle of the duct, the pressure field upstream of the fan stage is 180 degrees out of phase with the pressure field downstream of the fan stage. Thus, the sound radiates with the same intensity from the inlet and outlet. This can also be verified by observing Figures 5.9(a) and 5.9(b), which display the directivity of the sound pressure level in the far field of the duct inlet and outlet, respectively. The directivity plots exhibit a notch in the center (axis of the duct) that corresponds to the nodal line of the (1,0) mode pattern.

From theory, the axial wave number $k_z^{1,0}$ of the (1,0) mode is 4.65 m^{-1} at this frequency. The spectrum computed from pressure data collected in the inlet is presented in Figure 5.10. It exhibits a peak at $k_z = \pm 4.64\, m^{-1}$. The peak at $k_z = +4.64 m^{-1}$ corresponds to the mode (1,0) propagating towards the inlet opening, and the smaller peak at $k_z = -4.64 m^{-1}$ corresponds to the reflected wave. Referring to Eq. (4.42), these axial wavenumbers correspond to an angle of peak radiation of 22° for the (1,0) modes radiating from the duct inlet and outlet openings.

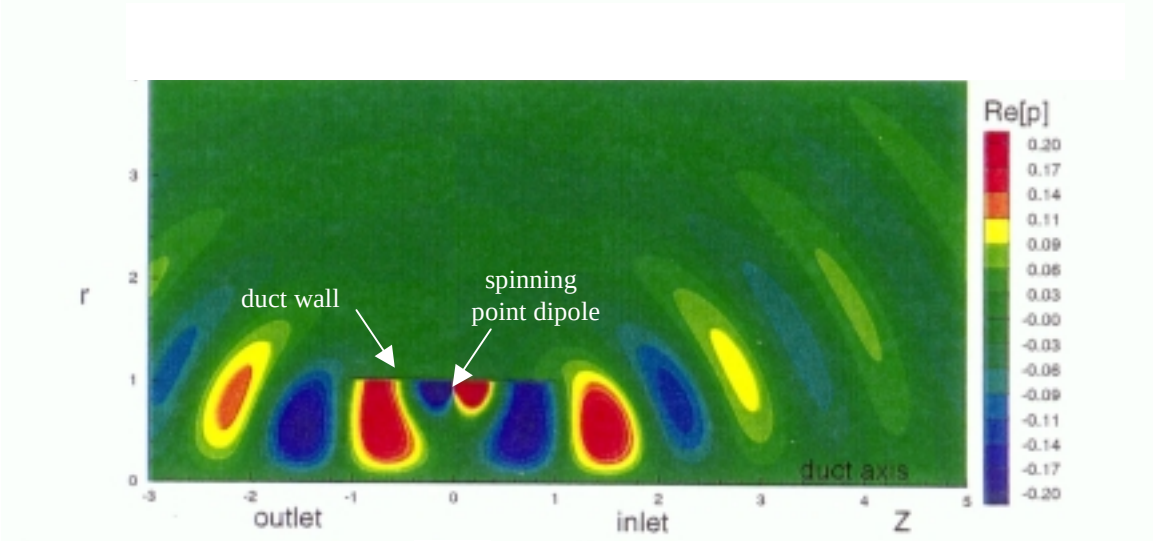

a) No control.

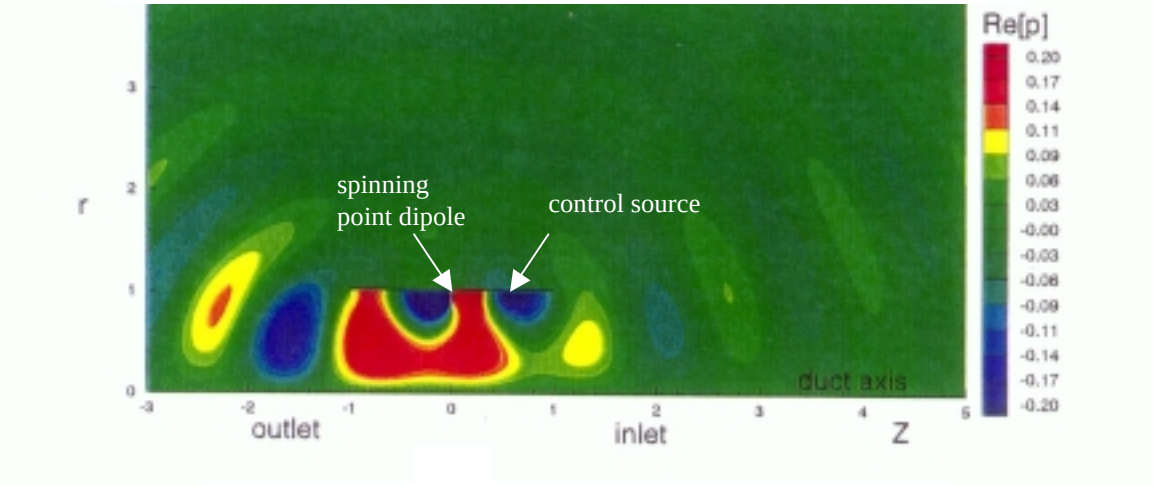

b) With active noise control. Single control array.

Figure5.8: Pressure field generated by the ducted fan. M=0, BPF=270 Hz.

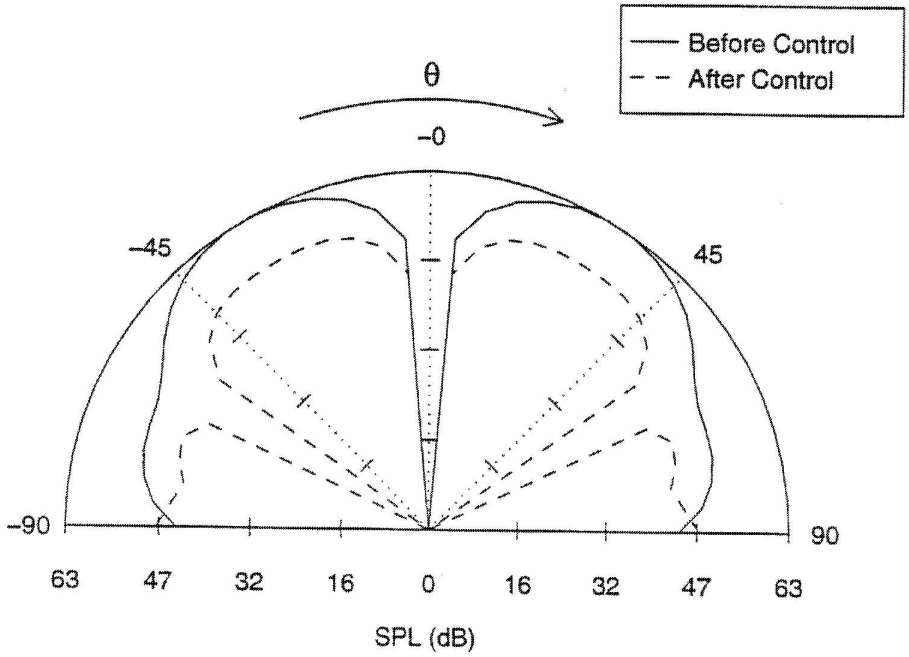

a) inlet

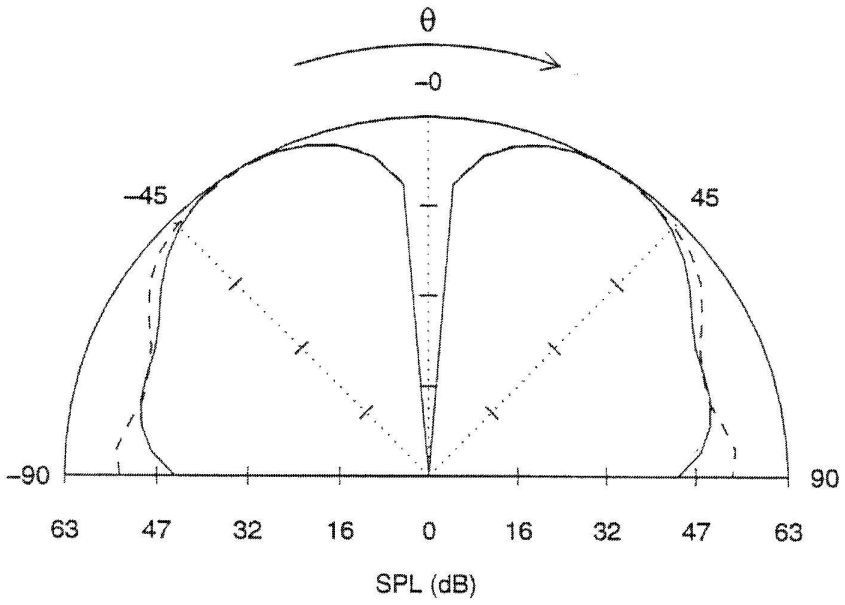

b) outlet

Figure 5.9: Radiation directivity of the controlled and uncontrolled fan noise using a single array of control sources and error sensors. M=0, BPF=270 Hz.

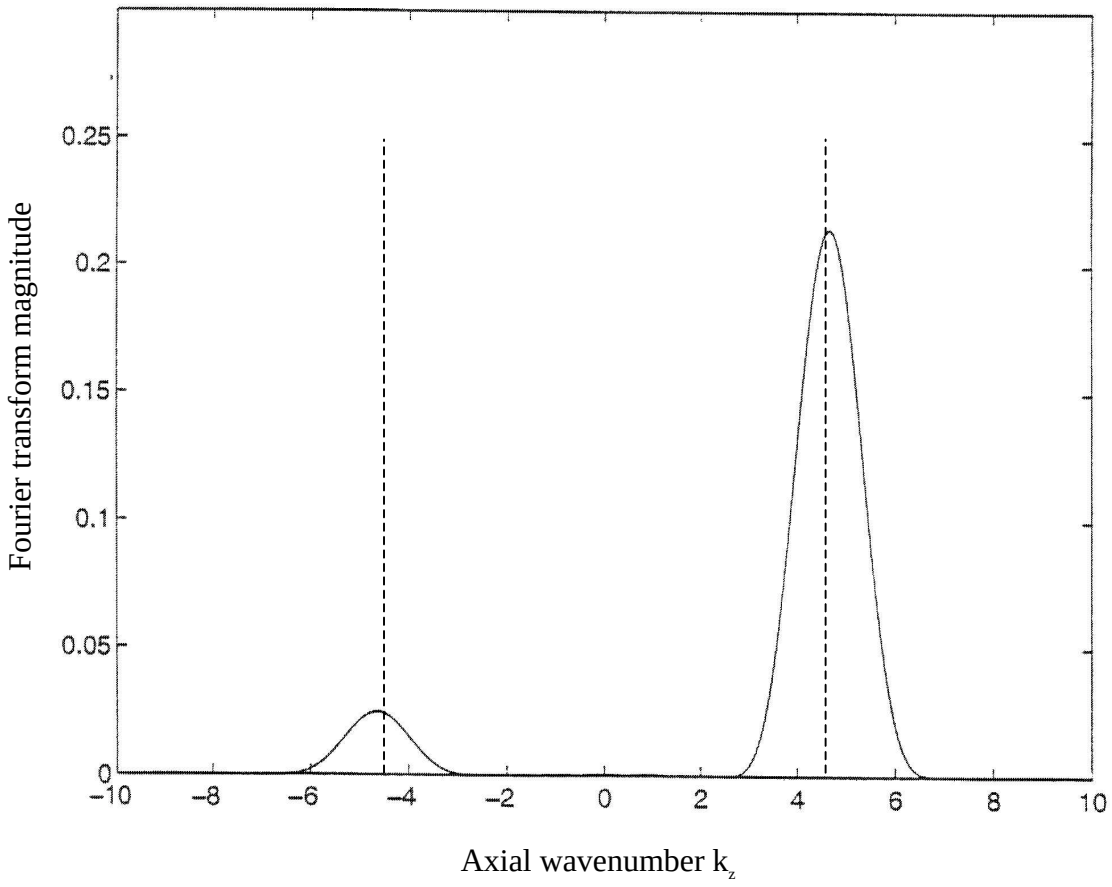

Figure 5.10: Spectrum of the inlet fan noise. M=0, BPF=270 Hz.

In an attempt to reduce the intensity of the sound radiated from the inlet, four control sources (i.e. point monopoles) are evenly spaced within the periphery of the inlet duct, in a single axial plane located upstream of the fan as described in Figure 5.11. The control sources are divided into 2 channels. The first control channel drives the first source located at 0° and the third source located at 180°, with a 180° phase difference. Similarly, the second control channel drives the second source located at 90° and the fourth source located at 270°, with a 180° phase difference. This configuration is selected for best coupling with the m=1 duct modes produced by the fan (Burdisso et al. 1994).

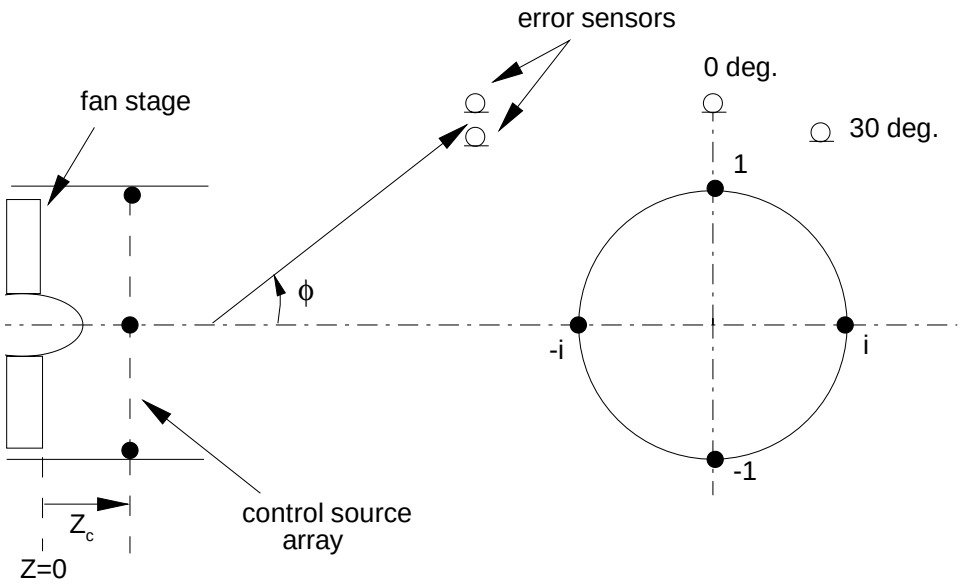

Figure 5.11: Schematic of the control system configuration. Single array of control sources and far field error sensors.

Two error sensors are placed in the far field around the engine axis with the first sensor at 10° and the second one at 30°. The error sensors are stepped through varying angular positions Φ as measured from the engine axis. In order to find the configuration of the control system that performs the best, the axial position of the control source array described earlier is stepped along the duct length from 0.1m to 0.9m upstream of the fan in 0.1 increments, while the angle Φ for the far field error sensors is also stepped from 10° to 90° with 10° increments.

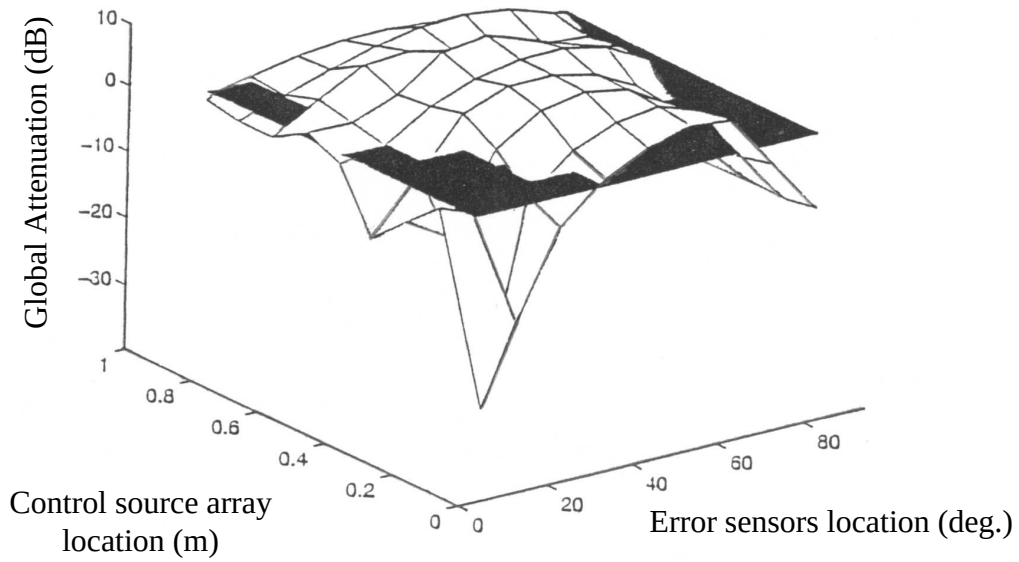

a) BPF=270 Hz

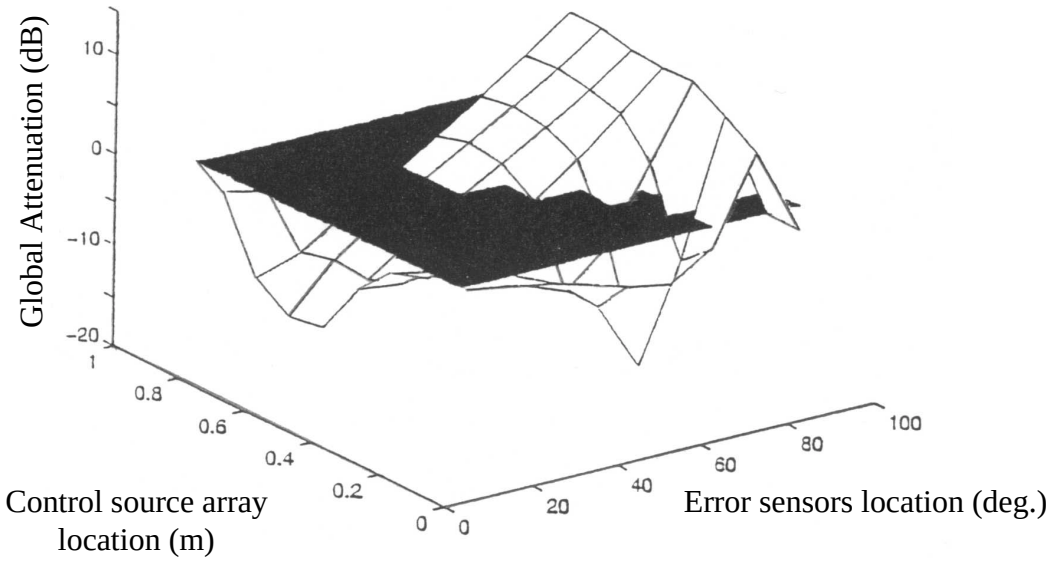

b) BPF=135 Hz

Figure 5.12: Global attenuation results achieved with a single array of control sources and far field error sensors.

The results are presented in Figure 5.12(a), which shows that the best global attenuation that could be achieved is 8.34 dB when the array of control sources is positioned 0.5 m upstream of the fan and the error sensors are at an angle Φ of 60° from the engine axis. Figure 5.8(b) displays the pressure field generated by the ducted fan and the control system that performed the best. It can observed as expected, a clear reduction in the intensity of the waves radiating from the fan inlet and an increase in the intensity of the wave radiating from the fan outlet (cf. Table 5.1).

Table 5.1: Radiated sound power level. Single array of control sources and error sensors. M=0, BPF=270 Hz.

	Sound power Level, dB	
	Inlet	**Outlet**
Before control	110.42	110.42
After control	102.05	111.02

It can also be seen from Figure 5.9(a) that global reduction of the fan noise was achieved and that complete noise cancellation was obtained at $\Phi = 60^\circ$, which is the angle where the error sensors were located. However, a global cancellation of the sound radiated through the duct inlet is not observed.

One reason for the non-global cancellation of the inlet radiation is the interference between the inlet and outlet radiation that is promoted by the overall short length of the duct. Thus, the error sensors placed in the far field of the inlet are registering the (1,0) mode that radiates from the inlet and the (1,0) mode that radiates from the outlet. The (1,0) modes that radiate respectively from the inlet and outlet, reach the error sensors with

different phases and amplitudes. Therefore, the active control system, comprised of a single control source array, is actually trying to control not one, but two modes (or degrees of freedom). This will of course decrease the performance of the control system.

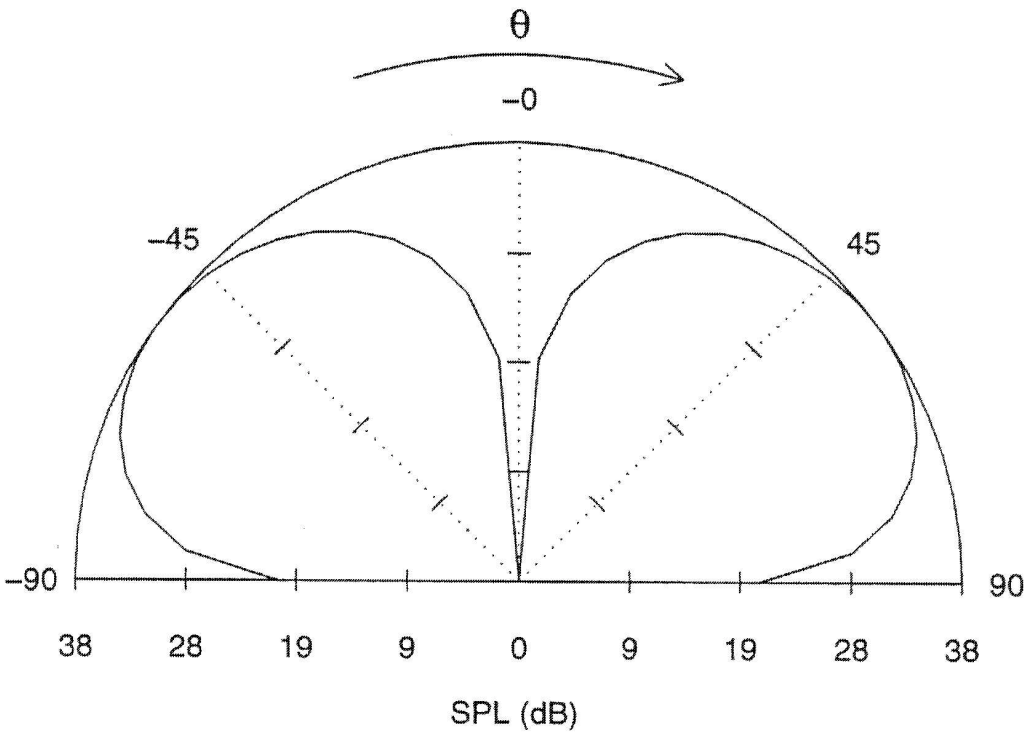

Figure 5.13: Radiation directivity of the inlet fan noise
when all modes are cut off. M=0, BPF=92 Hz.

Another reason for the non-global cancellation of the sound radiated through the inlet can be understood by observing Figure 5.13, which depicts the radiation of the sound in a case where all the modes are cut off. This radiation is seen to be substantial. This is due to the short length of the inlet (L/2) which prevents the modes that are cut off from completely decaying before reaching the inlet opening, thus allowing them to radiate into

the far field. This phenomenon is illustrated in Figure 5.14 and described in more detail bellow.

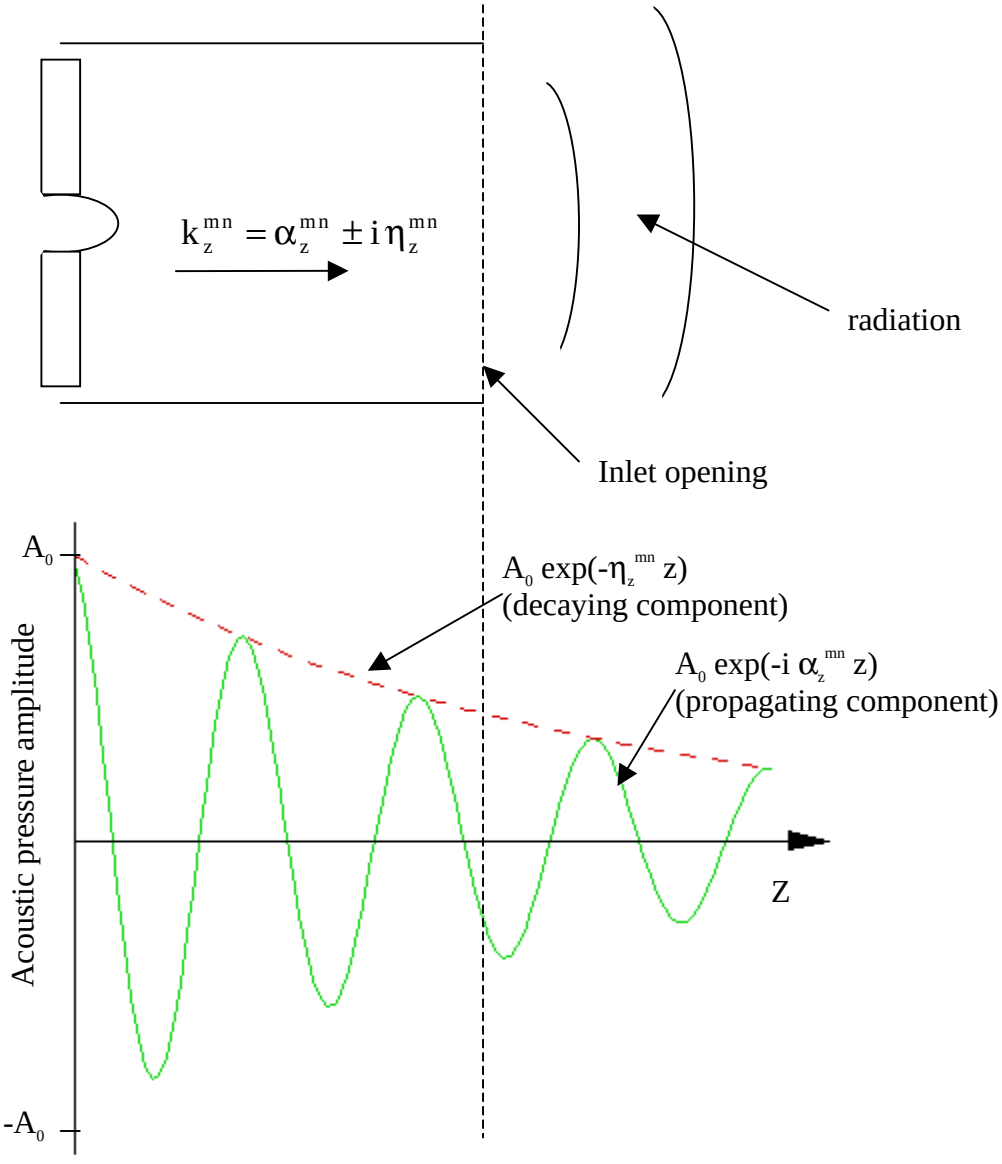

Figure 5.14: Radiation of evanescent modes to the acoustic far field.

As mentioned earlier in chapter 3, a mode decays when its axial wavenumber k_z^{mn} is imaginary, i.e., when k_z^{mn} is of the form

$$k_z^{mn} = \alpha_z^{mn} \pm i\eta_z^{mn} \quad , \quad \eta_z^{mn} \rangle 0 \, . \tag{5.4}$$

Hence, referring to Eq. (3.1), at a given radial and angular location in the duct and at a given time t_0, the acoustic pressure of a mode decaying in the duct is of the form

$$p_{mn}(r_0, \psi_0, z, t_0) = A_0(r_0, \psi_0, t_0) \exp(-i\alpha_z^{mn} z) \exp(-\eta_z^{mn} z) \tag{5.5}$$

(The positive imaginary part of k_z^{mn} in Eq. (5.4) is ignored in order to keep the solution for the acoustic pressure bounded). Thus, if a mode is bellow its cut on frequency, its magnitude will decrease exponentially as it propagates through the duct and, as illustrated in Figure 5.14, will radiate if it does not completely decay before reaching the duct opening.

From Eq. (5.5), it is seen that a mode that is cut off decays faster as the magnitude of the imaginary part of k_z^{mn} increases. In the case where the flow Mach number is 0, the axial wave numbers of the modes that are decaying are purely imaginary and their magnitudes increase as the wave number k decreases. Therefore, by lowering the fan tip Mach number (and therefore lowering the wave number), the radiation of the near field into the far field is reduced because the modes that are cut off decay faster. Thus, reducing the blade passage frequency from 270Hz to 135Hz, we recompute the attenuation of the radiated sound power that can be achieved for different axial locations of the control source array and different angular location of the error sensors. The results are presented in Figure 5.12(b). It can be seen that the best global attenuation that could be achieved is 12.72 dB, versus 8.34 dB in the previous case. This is an improvement of 4.38 dB. This seems to corroborate the idea that the near fields from the control sources and the fan affect the performance of the active noise control system, which is an important observation.

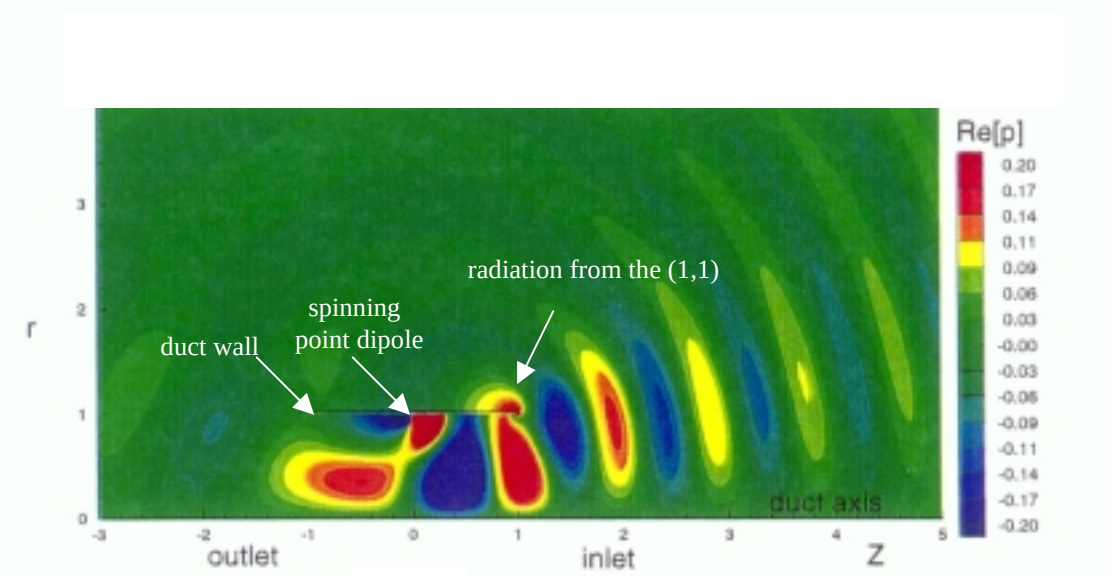

a) No control.

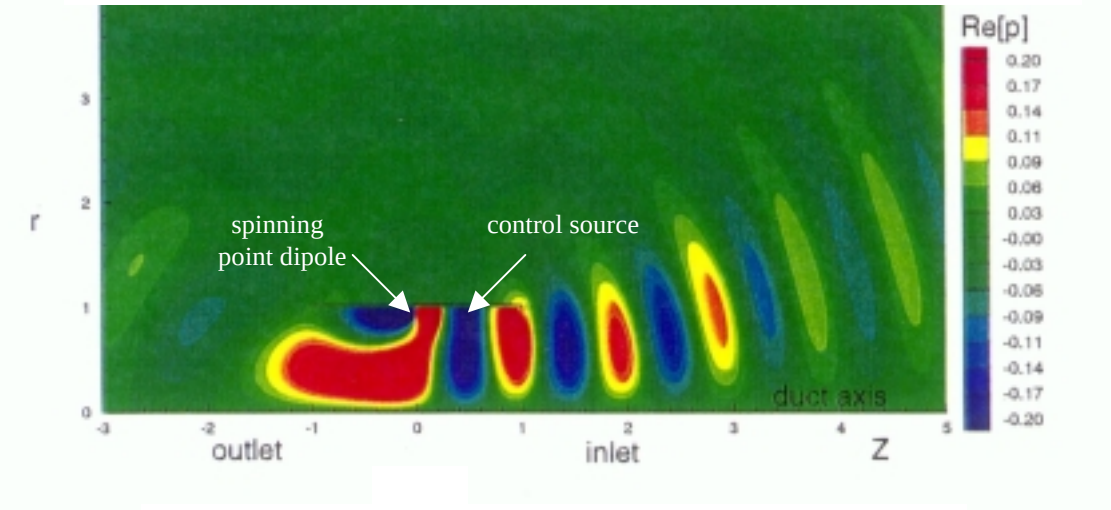

b) With active control. Single array of control sources.

Figure 5.15: Pressure field generated by the ducted fan. M=0.3, BPF=270 Hz.

5.3.2 Moving duct with a single array of control sources

The duct is now assumed to be translating in the axial direction with a uniform velocity (this is equivalent to considering the duct as stationary and immersed in a uniform flow). The forward flight Mach number is 0.3 and the blade passing frequency is unchanged (270 Hz). The pressure field generated by the ducted fan is presented in Figure 5.15(a). In this figure, the sound is seen to radiate more strongly from the inlet than from the outlet. This is due to the fact that when a sound source is in motion, the pressure perturbation in the forward arc is more intense than that in the rear arc. This phenomenon is known as the Doppler effect and is explained next when considering the simple example of a point monopole translating with a uniform velocity V in a medium at rest, as illustrated in Figure 5.16.

The pressure field generated by a point monopole of strength q(t) is given by (Dowling and Ffowcs William 1983)

$$p(x, y, z, t) = \frac{q(\tau)}{4\pi r(\tau)} \tag{5.6}$$

where $r(\tau)$ is the distance between the fixed observer and the moving source and τ, the retarded time (or time of sound emission), is equal to $t - r(\tau)/c$. In order to better display the effects of source motion, Eq. (5.6) is rewritten as

$$p(x, y, z, t) = \int_{-\infty}^{+\infty} \frac{q(\tau)}{4\pi r(\tau)} \, \delta\left(t - \frac{r}{c} - \tau\right) \, d\tau . \tag{5.7}$$

Now, noting that for any functions f,g,

$$\int_{-\infty}^{+\infty} f(\tau) \, \delta(g(\tau)) \, d\tau = \left[\frac{f(\tau)}{|dg / d\tau|} \right]_{\tau=\tau^*}, \tag{5.8}$$

where τ^* is a zero of g, the integral in Eq. (5.7) can be evaluated. In this case, $g = t - r/c - \tau$ and

$$\frac{dg}{d\tau} = -(1 - M_r) \tag{5.9}$$

where M_r is the resulting component of the source velocity in the direction of the observer. In the present case, $M_r = M \cos\theta$ where $M = V/c$ and θ is the angle between the position of the observer and the axis of translation of the point monopole, measured from the source position at emission time. Applying Eq. (5.8) to Eq. (5.7) yields

$$p(x, y, z, t) = \frac{q(\tau^*)}{4\pi r(\tau^*)\,|1 - M\cos\theta|} \tag{5.10}$$

where τ^* satisfies $c(t - \tau^*) = r(\tau^*)$. The above equation is an expression for the acoustic pressure measured by the observer at time t and emitted by the moving source at time τ^*. It can be seen from Eq. (5.10) that where the source is at rest, the emitted sound field is omnidirectional. The factor $(1 - M\cos\theta)^{-1}$ means that when the sound source is in motion, there is a reinforcement of the sound intensity as the source approaches the point of observation and a diminution of the sound intensity in the opposite case (Doppler effect). This effect which occurs for any arbitrary motion of a sound source, is observed in the present case as a longitudinal point dipole translates in its axial direction while spinning around the axis of the duct.

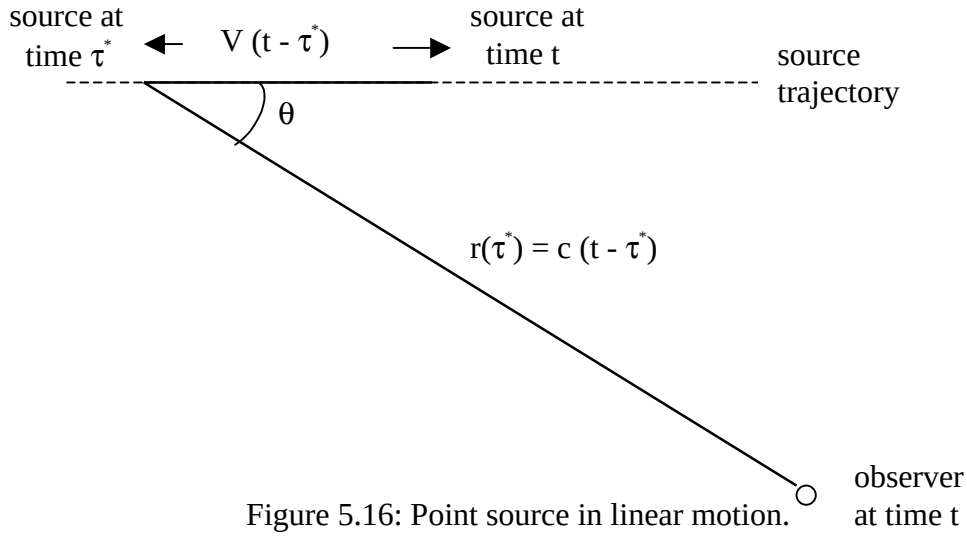

Figure 5.16: Point source in linear motion.

Referring to Eq. (3.2), at a flight Mach number of 0.3, the (1,0) mode is still the only mode cut-on. From duct theory (Mofrey 1964), it propagates upstream with an axial wave number $k^{1,0}_{(+),Z} = +6.79\,m^{-1}$, and downstream with an axial wave number $k^{1,0}_{(-),Z} = -3.49\,m^{-1}$. Referring to Eq. (4.42), these axial wavenumbers correspond to an angle of peak radiation of 37.6° for the (1,0) modes radiating from the duct inlet and outlet openings. Figure 5.17 displays the spectrum computed from data collected in the duct inlet.

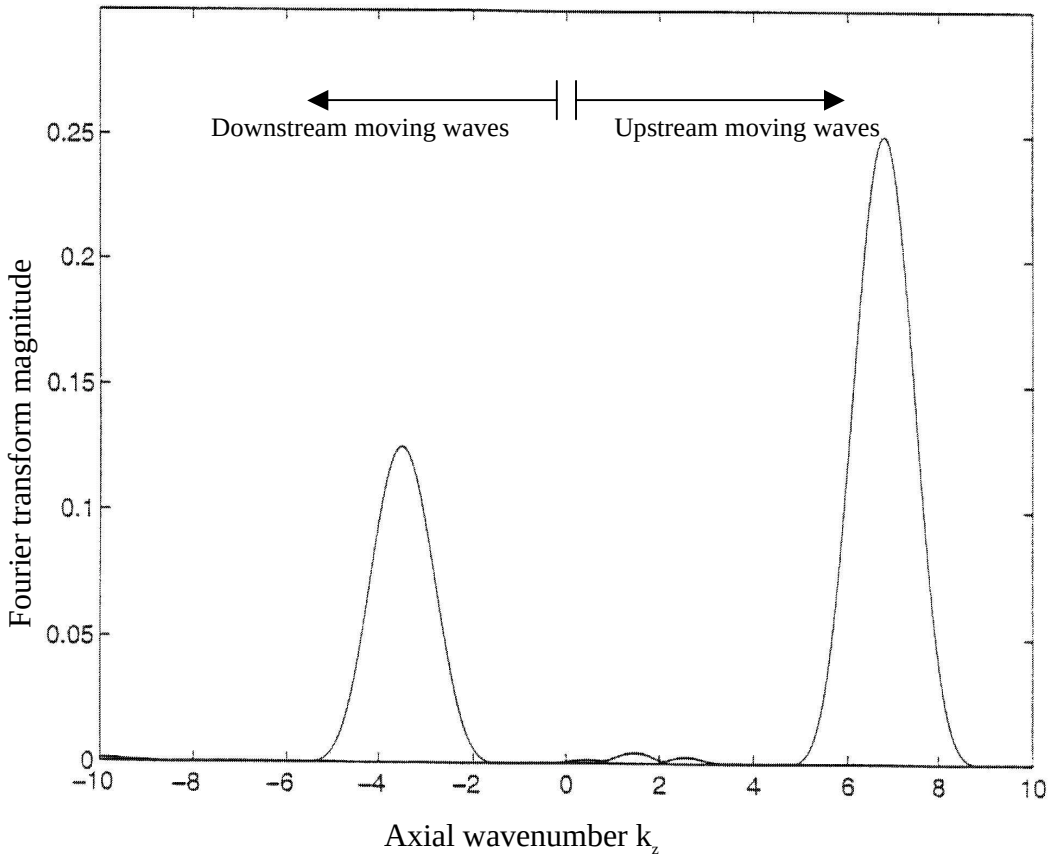

Figure 5.17: Spectrum of the inlet fan noise. M=0.3, BPF=270 Hz.

This spectrum exhibits the expected peaks at $k_Z = +6.79\,m^{-1}$ and $-3.49\,m^{-1}$, as well as a small peak at $k_Z = +1.64\,m^{-1}$ corresponding to the oscillatory component of the (1,1) mode, which is very close from being cut on. Thus, referring to Eq. (3.2) and Eq. (3.7), the axial wavenumber and cut-off ratio of the (1,1) mode are, respectively, $k_z = 1.64 + 0.95\,i$ and $\xi^{1,1} = 0.98$ (a mode is cut on when its cut-off ratio is equal to or greater than 1). Referring to Eq. (3.1) and Eq. (3.5), the disturbance pressure field in the duct corresponding to the (1,1) mode is of the form $A_{1,1}\, J_1(5.33\, r) \exp(-i\, 1.64\, z) \exp(-0.95\, z) \exp(i\, m(\Omega t - \psi))$, where $\exp(-0.95\, z)$ is the decaying factor. Hence, when it reaches the inlet opening, the (1,1) evanescent mode has decreased in magnitude by a factor of only 0.38 and, as seen in Figure 5.15(a), it weakly radiates toward the sideline of the duct.

A single array of control sources and two far field error sensors are again used in an attempt to reduce the sound radiation from the duct inlet. The phasing and placement of the control sources within the circumferential array is the same as in the preceding case, and the error sensors are still placed respectively at 10° and 30° around the engine centerline. The angle Φ that the two error sensors make with the engine centerline, as well as the axial location of the control source array within the duct inlet are re-optimized in order to obtain to a maximum reduction of the sound power level radiating from the duct inlet. The best performance of the control system is achieved when the error sensors are at an angle $\Phi = 70^\circ$ from the duct axis, and when the control source array is placed 0.4 m upstream of the fan.

The results are presented in Figure 5.15(b), Figure 5.18(a), and Figure 5.18(b). The pressure notch at the error sensor location is visible, along with a reduction of the fan noise in the sideline regions. However, unlike the stationary duct case, no reduction of the radiated pressure could be obtained in the central regions without generating considerable sideline spillover. This is probably caused by the radiation from the (1,1) evanescent mode and by the fact that wall mounted control sources are more effective in putting

energy into the higher order radial modes (Smith et al. 1997). Thus, in order to reduce effectively the intensity of the pressure that radiates toward the front of the engine (i.e., better control of the radiation from the (1,0) mode), the error sensors have to be placed closer to the direction of peak radiation of the (1,0) mode. By doing so, most of the energy that the control sources put out to cancel the noise at the error sensors location goes into the (1,1) evanescent mode generated by the control source array, instead of into the (1,0) control mode. This (1,1) evanescent mode then reinforces the sideline radiation of the (1,1) mode generated by the fan, while the radiation from the (1,0) mode is only slightly reduced. This interaction thus results in an overall increase of the sound power level radiated from the inlet.

The global reduction in sound power level achieved in the far field of the inlet for the present case was of 2 dB; that is 6 dB less than what was achieved with the same control system configuration in the stationary case (see Table 5.1 and Table 5.2).

Table 5.2: Radiated sound power level. Single array of control sources and error sensors. M=0.3, BPF=270 Hz.

	Sound power Level, dB	
	Inlet	**Outlet**
Before control	112.06	104.92
After control	111.13	105.4

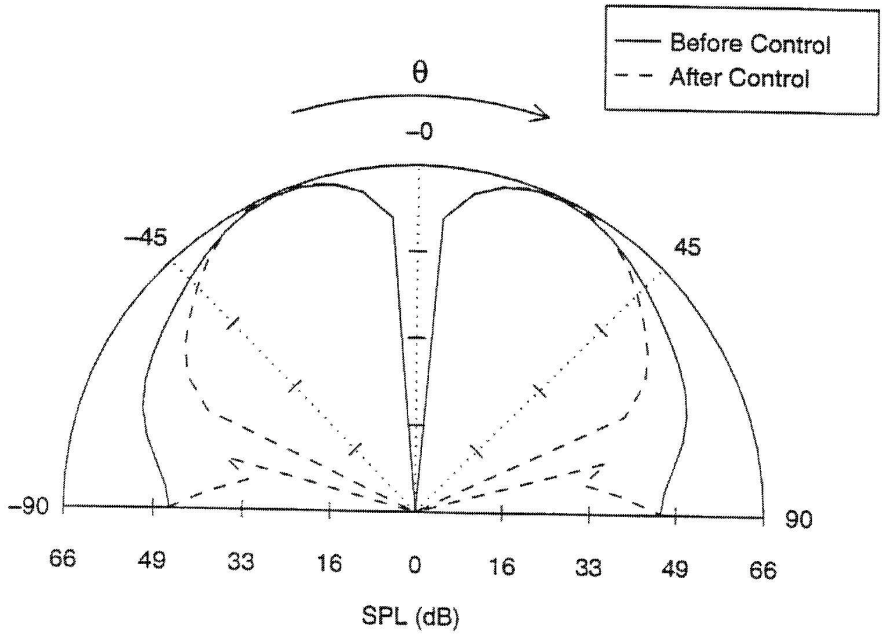

a) inlet

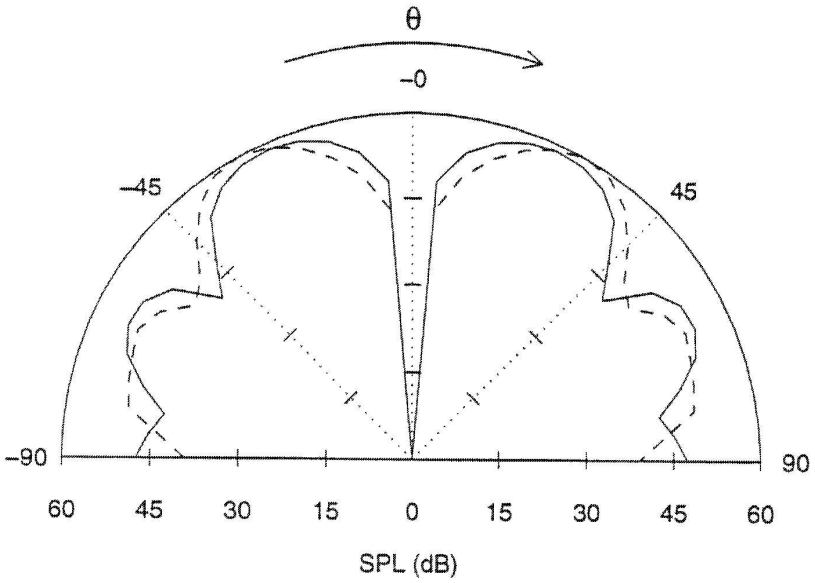

b) outlet

Figure 5.18: Radiation directivity of the controlled and uncontrolled fan noise using a single array of control sources and error sensors. M=0.3, BPF=270 Hz.

These results are now compared to the ones that are obtained when the flight Mach number is 0.5 instead of 0.3. The control system configuration (i.e., the axial location of the control source array and the angular location Φ of the error sensors) is re-optimized. The results obtained in this case are presented in Figures 5.19(a) and 5.19(b) and Figures 5.20(a) and 5.20(b). A reduction of 1dB of the sound power level was achieved in the far field of the inlet (cf. Table 5.3). However, Figure 5.19(b) and Figure 5.20(a) reveal that considerable sideline spillover has been generated. From Eq. (3.7), it is found that both the (1,0) and (1,1) modes are cut on. The cut-off ratio of the (1,0) and (1,1) modes are respectively 3.13 and 1.08. The poor performance of the control system is therefore due to the presence of the additional mode radiating from the inlet. The active control system, comprised of a single control source array, is now trying to control a system of not one, but two degrees of freedom (or four degrees of freedom if, as explained earlier in section 5.3.1, the modes that radiate from the outlet are included). To improve the performance of the control system, multiple axial control source arrays are required.

The spectrum obtained from the fan noise in the duct inlet is displayed in Figure 5.21. This spectrum exhibits four peaks. Eq. (3.2) indicates that the peaks located at $k_z = +9.89\,m^{-1}$ and $k_z = -3.22\,m^{-1}$ correspond to the (1,0) mode propagating upstream and downstream respectively, while the peaks at $k_z = +6.41\,m^{-1}$ and $k_z = +0.25\,m^{-1}$ correspond to the (1,1) mode propagating upstream with two different wave numbers. The situation in which a mode has two upstream moving phases (Eversman 1970(a)) can occur when the mode is close to its cut on frequency, as in the present case. Eversman demonstrated that in such a case, the acoustic energy is still being transferred to downstream and upstream regions (Eversman 1970(b)).

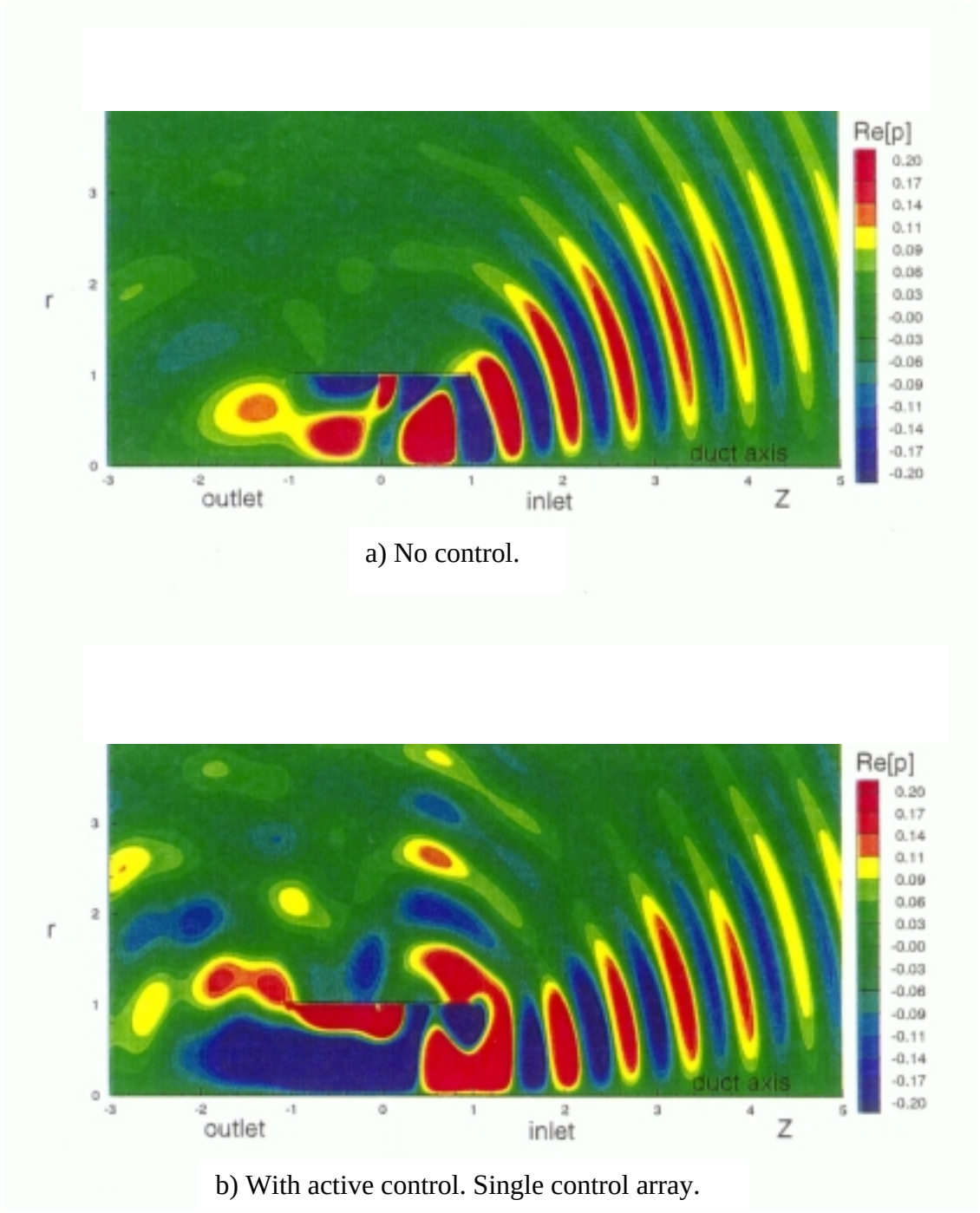

a) No control.

b) With active control. Single control array.

Figure 5.19: Pressure field generated by the ducted fan. M=0.5, BPF=270 Hz.

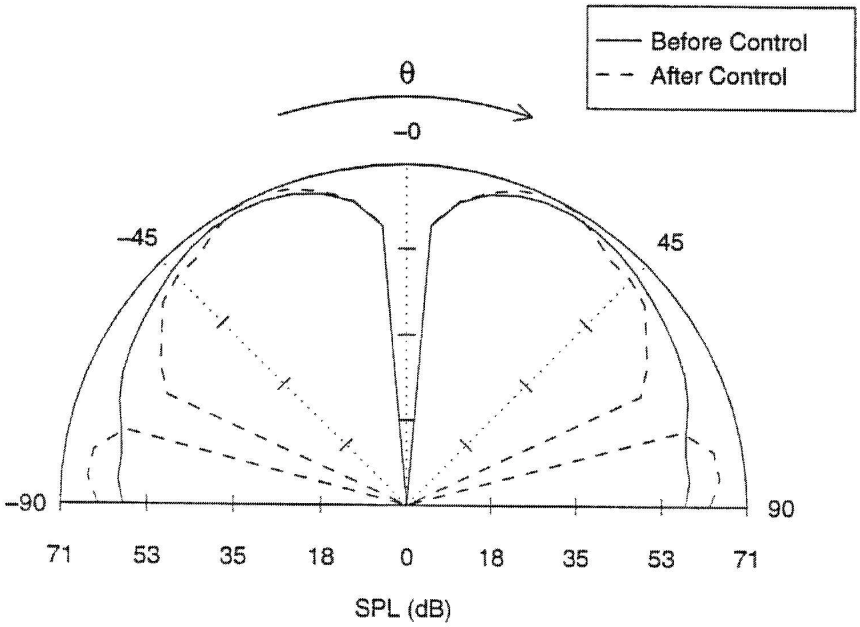

a) inlet

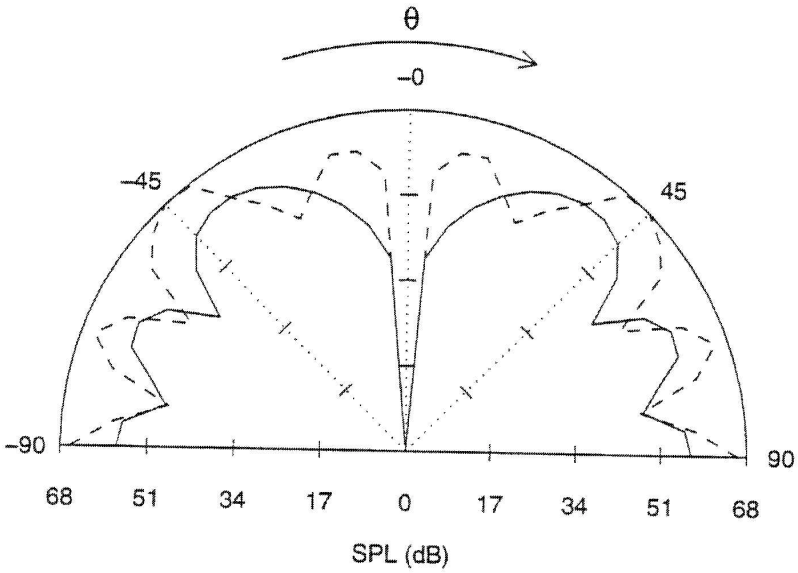

b) outlet

Figure 5.20: Radiation directivity of the controlled and uncontrolled fan noise using a single array of control sources and far field error sensors. M=0.5, BPF=270 Hz.

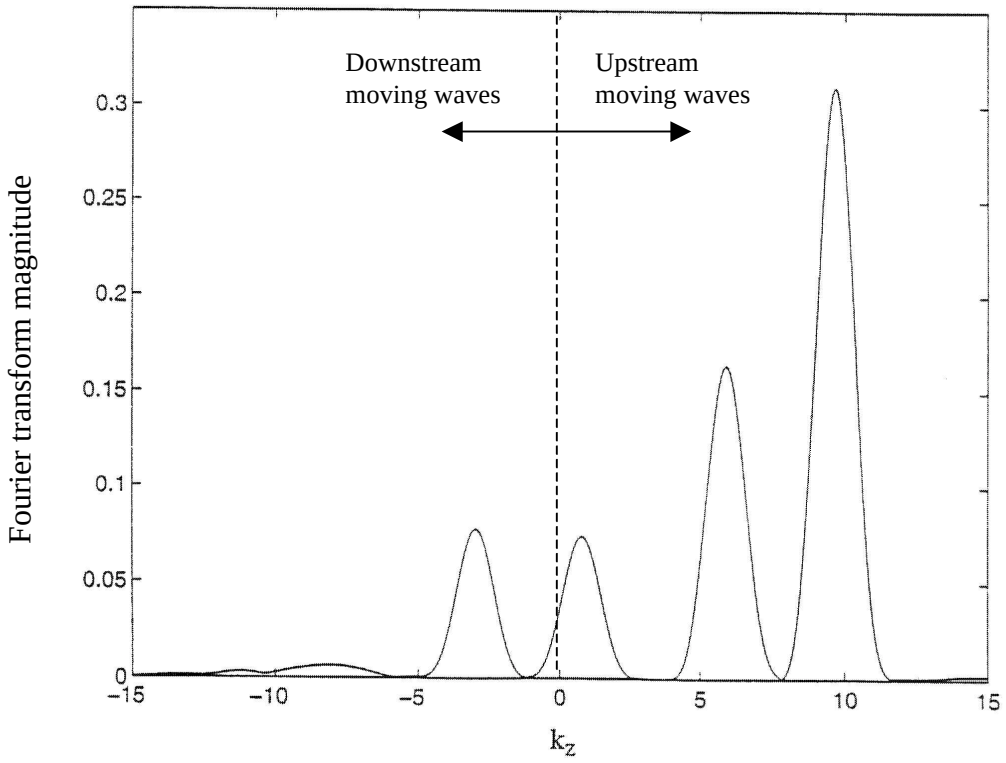

Figure 5.21: Spectrum of the inlet fan noise. M=0.5, BPF=270 Hz.

Table 5.3: Radiated sound power level. Single array of control sources and error sensors. M=0.5, BPF=270 Hz.

	Sound power Level, dB	
	Inlet	**Outlet**
Before control	117.64	109.17
After control	117.1	114.9

5.3.3 Stationary duct with multiple arrays of control sources

Multiple arrays of control sources placed at different axial locations within the duct is a configuration of the active control system that is especially used when radial modes are targeted for control. The intent here is not to demonstrate why and when multiple arrays of control sources are used, but only to show that such a configuration can be implemented to the model. Thus, for this third case, the duct is chosen to be stationary, and the blade passing frequency is increased from 270 Hz to 325 Hz such that the (1,0) and (1,1) modes are cut on. The resulting pressure field can be seen in Figure 5.22(a). It is observed in this figure that since the duct is stationary and since the spinning point dipole is centered between the inlet and outlet openings, the pressure field upstream of the fan stage is 180 degrees out of phase with the pressure field downstream of the fan stage. Hence, the sound radiates with the same intensity from the inlet and outlet.

The spectrum calculated from data collected in the duct inlet is presented in Figure 5.23. This spectrum displays two main peaks, the first one at $k_Z = +5.71\,m^{-1}$, and the second one at $k_Z = +2.75\,m^{-1}$ corresponding respectively to the (1,0) and (1,1) modes that are cut on and propagating towards the inlet opening. The smaller peaks at $k_Z = -5.71\,m^{-1}$ and $k_Z = -2.75\,m^{-1}$ correspond to the reflected waves. Referring to Eq. (4.42), these axial wavenumbers correspond to angles of peak radiation of 17.8° and 62.7° for the (1,0) and (1,1) modes, respectively. This spectrum shows the relative strengths of propagated and reflected waves. It indicates that the magnitude of the reflected (1,0) mode is about one third of the magnitude of the incident (1,0) mode, and that the magnitude of the reflected (1,1) mode is almost half of the magnitude of the incident (1,1) mode. Thus, in the present case (as well as in the cases presented previously in section 5.3.1 and 5.3.2), reflections from the inlet opening are substantial and could not be neglected since they are bound to affect the performance of the control system.

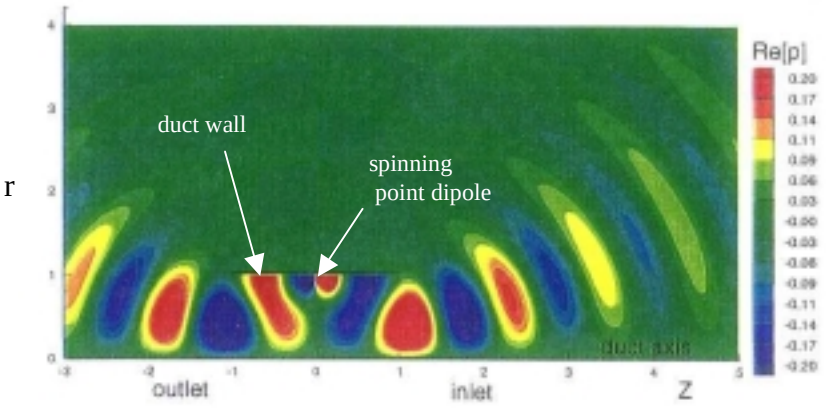

a) without control

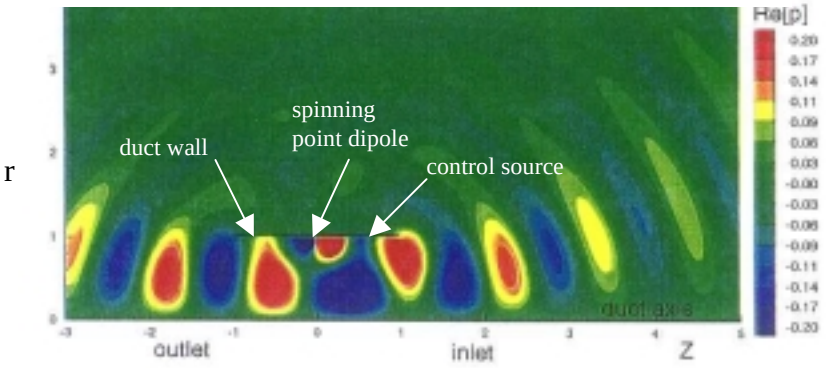

b) with control using a single array of control sources and error sensors

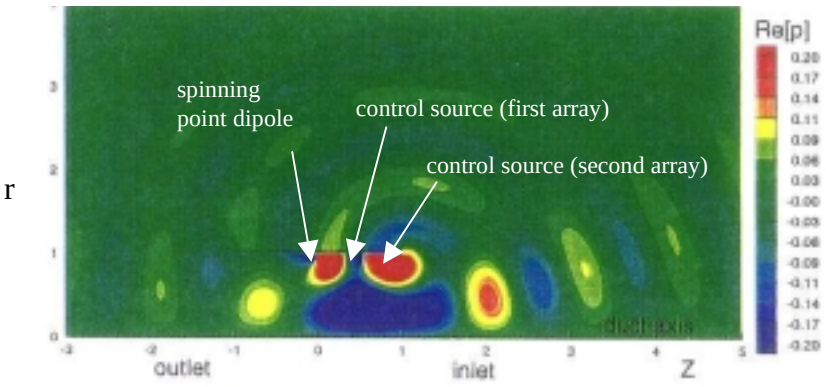

c) with control using 2 arrays of control sources and error sensors

Figure 5.22: Pressure field generated by the ducted fan. M=0, BPF=324 Hz.

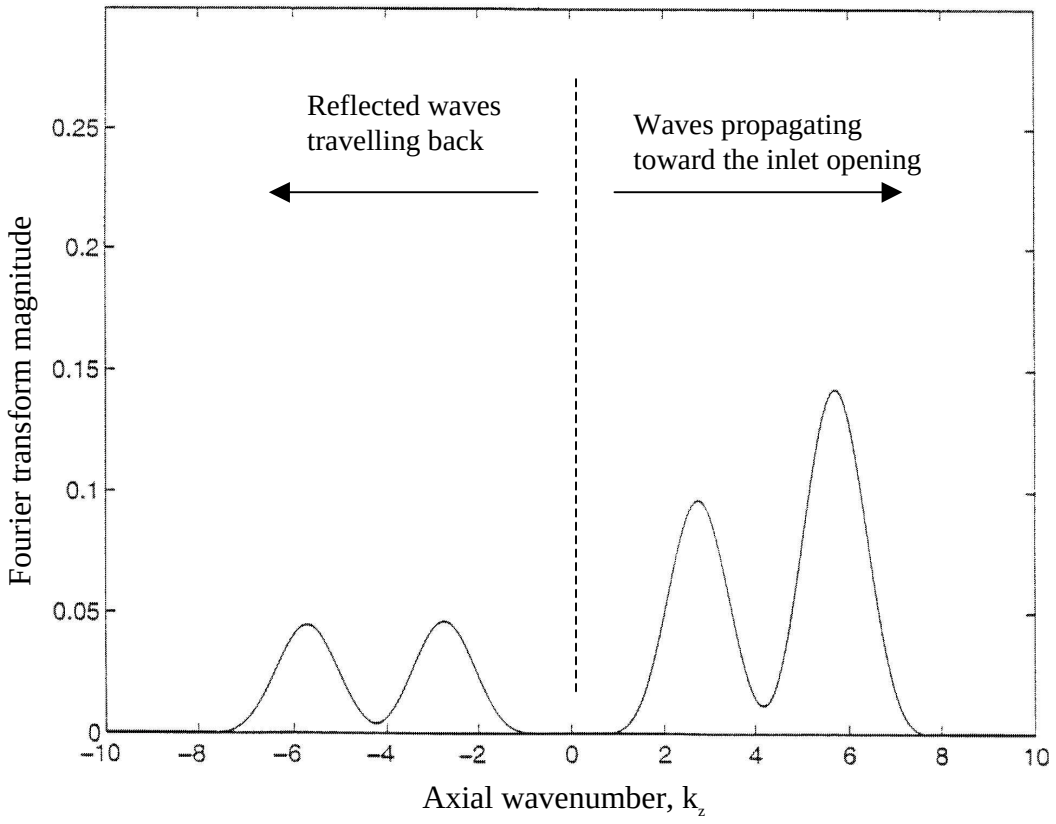

Figure 5.23: Spectrum of the inlet fan noise. M=0, BPF= 324 Hz.

The configuration of the control system is shown Figure 5.24. It is composed of two axial arrays of control sources each composed of four control sources grouped into two control channels and phased in the same manner described in cases 1 and 2. Four error sensors are placed in the far field as described in Figure 5.24. The first two error sensors are placed at an angle Φ_1 of 50° from the engine axis, while the second set of error sensors is placed at an angle Φ_2 of 60°. The control source arrays are placed

respectively 0.5 m and 0.6 m upstream of the fan. This configuration of the control system was chosen somewhat arbitrarily, the present purpose, as mentioned earlier, being only to demonstrate that multiple arrays of control sources can be implemented to the model. The results obtained with this configuration of the control system are presented in Figure 5.22(c) and in Table 5.4. They are compared to the best results that could be obtained when only a single array of control source and error sensors is used to perform noise control. These results are displayed in Figure 5.22(b) and in Table 5.4.

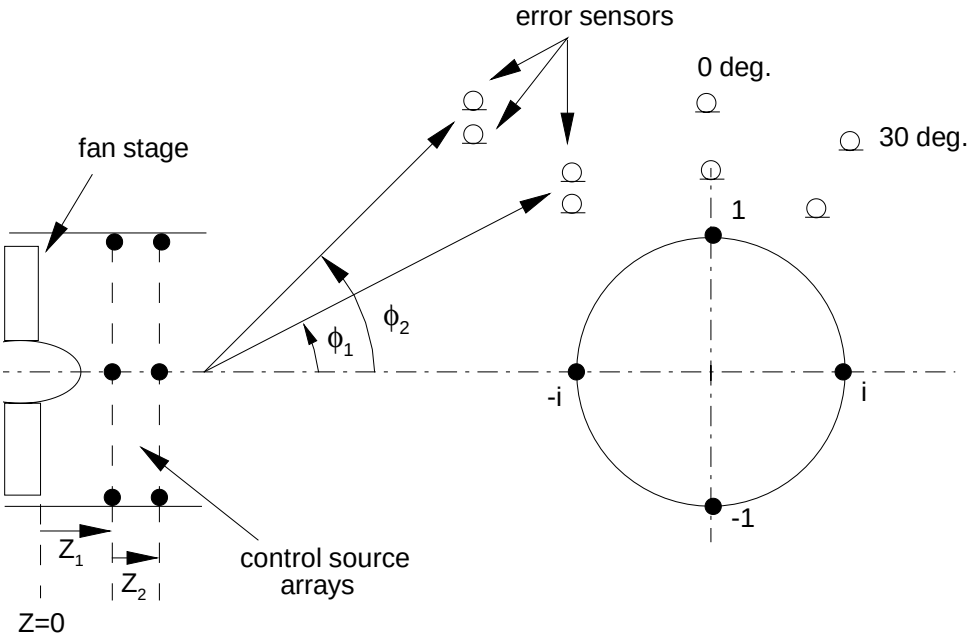

Figure 5.24: Schematic of the control system configuration.
Multiple arrays of control sources and far field error sensors.

Table 5.4: Radiated sound power level. Single array of control sources and error sensors. M=0, BPF=324 Hz.

	Sound power Level, dB	
	Inlet	**Outlet**
Before control	111.67	111.67
After control, single array	109.9	111.52
After control, 2 arrays	108.13	109.04

In the case where two arrays of control sources and error sensors are used, it is observed from Figure 5.20(c) that the sound field generated by the control sources destructively interferes with the fan noise radiating from the inlet, as well as with the fan noise radiating from the outlet. Thus, although the (1,0) and (1,1) fan modes radiating from the inlet are primarily targeted for control (since the error sensors are placed in the far field of the inlet), the configuration of the control system is such that the (1,0) and (1,1) control modes propagating toward the outlet also destructively couple with the fan modes that propagate in the same direction. Note, however, that other configurations of the control system (i.e., a different positioning of the control arrays and error sensors) could have led to a reinforcement of outlet radiation.

Comparing Figure 5.22(b) with Figure 5.22(c), it can be seen clearly that the reduction in sound pressure level achieved in the far field of the inlet with the multiple arrays configuration of the control system is greater than the one achieved with a single array configuration. Thus, referring to Table 5.4, a reduction of 3.54 dB in sound power

level was obtained in the far field of the inlet when using two control source arrays, compared to a maximum reduction of only 1.77 dB when a single control source array was used. This difference in performance between the two control systems results from the larger coverage of the far field by the error sensors with the multiple arrays configuration, as well as from the fact that use of multiple control source arrays increases the controllability of a system having multiple degrees of freedom.

5.4 Conclusions

The analytical derivation and numerical implementation of the fan and control source models were validated. The good agreement between the numerical and experimental results presented in section 5.1 shows that the fan models considered in this study can provide a good simulation of actual engine fan noise in the instance where the modal amplitude of the propagating modes, or the loading force distribution on the fan blades, is known.

The preliminary results obtained from the demonstrative cases of active noise control that were performed indicate that: 1) The model is conducive to more realistic studies of active noise control on ultra high bypass turbofan engines because it accounts for evanescent modes generated by the fan and control sources, and for the interference between inlet and outlet radiation, which were shown to have some impact on the performance of the active noise control system. 2) The model is useful, it provides some insight into the behavior of the pressure field downstream of the outlet and around the duct, when active noise control of inlet noise is performed. Thus, it was observed that although control of the inlet noise was, in most of the test cases done, leading to a slight increase of the outlet noise, simultaneous reduction of both inlet and outlet noise can be obtained. 3) The model is computationally efficient, and therefore suitable for conducting parametric studies.

Additional insights into active noise control of UHB engines were provided by the preliminary results. Thus, regarding the influence of the flight Mach number on the ANC system performance, it was observed that an increasing number of radial modes are cut on and radiate through the duct inlet as the flight Mach number increases, making control of the inlet noise more difficult and the use of multiple axial arrays of control sources necessary. Finally, the apparent impact that the near field has on the performance of the control system suggests that a passive control of the decaying modes in the duct would be useful.